Au–Ag Core–Shell Nanoparticle Array by Block Copolymer Lithography for Synergistic Broadband Plasmonic Properties

Seung Keun Cha,[†,‡] Jeong Ho Mun,[†] Taeyong Chang,[†] Sang Yun Kim,[†,‡] Ju Young Kim,[†,‡] Hyeong Min Jin,[†,‡] Jeong Yong Lee,[†,‡] Jonghwa Shin,[†] Kwang Ho Kim,[*,§] and Sang Ouk Kim[*,†]

[†]Department of Materials Science & Engineering, Korea Advanced Institute of Science and Technology (KAIST), Daejeon 305-701, Republic of Korea, [‡]Center for Nanomaterials & Chemical Reactions, Institute for Basic Science (IBS), Daejeon 305-701, Republic of Korea, and [§]Department of Materials Science & Engineering, Pusan National University, Pusan 609-735, Republic of Korea

ABSTRACT Localized surface plasmon resonance of metallic nanostructures receives noticeable attention in photonics, electronics, catalysis, and so on. Core–shell nanostructures are particularly attractive due to the versatile tunability of plasmonic properties along with the independent control of core size, shell thickness, and corresponding chemical composition, but they commonly suffer from difficult synthetic procedures. We present a reliable and controllable route to a highly ordered uniform Au@Ag core–shell nanoparticle array *via* block copolymer lithography and subsequent seeded-shell growth. Size-tunable monodisperse Au nanodot arrays are generated by block copolymer self-assembly and are used as seed layers to grow Ag shells with variable thickness. The resultant Au@Ag core–shell nanoparticle arrays exhibit widely tunable broadband enhancement of plasmonic resonance, greatly surpassing single-element nanoparticle or homogeneous alloy nanoparticle arrays. Surface-enhanced Raman scattering of the core–shell nanoparticle arrays showed an enhancement factor greater than 270 from Au nanoparticle arrays.

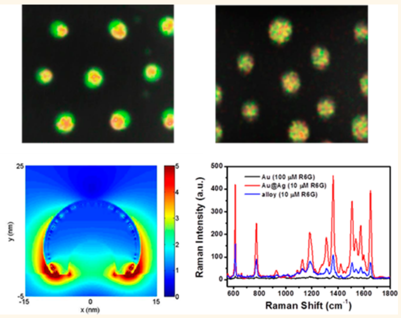

KEYWORDS: block copolymer · nanoparticle · plasmon · bimetal · self-assembly

Noble metal nanoparticles (NPs), such as gold (Au) and silver (Ag), exhibit unique optical properties arising from localized surface plasmon resonance (LSPR),[1−7] which can be utilized for bioimaging,[8−10] optical sensing,[7,11] catalysis,[12,13] surface-enhanced Raman scattering (SERS),[14−18] and so on. Core–shell bimetallic NPs consisting of two different metallic elements are particularly attractive due to the precise controllability of their structures and properties. Independent control of the core size, shell thickness, chemical composition, and interparticle distance offers versatile routes to control the plasmonic resonance wavelength, strength, and broadness.[7,18−21] Additionally, synergistic interplay between different metallic components may greatly strengthen the resonance properties.

Presently, metal NPs are principally prepared by solution-phase synthesis. Conventional solution synthesis requires a high-temperature reaction to burst nucleation, suitable surfactants to avoid aggregation, and solvent change or several centrifugations for narrow size distribution. The synthesis of multimetallic NPs is even more complicated due to the subtle manipulation of different metal precursors.[22] While various synthetic methods, such as co-reduction,[23−26] thermal decomposition,[27,28] and galvanic replacement reaction,[29−31] are explored for multimetallic NP synthesis, "seeded growth" provides a unique way to peculiar structures, such as core–shell structures.[19,32−34] In this approach, it is crucial to nucleate the seeds with uniform shape and size for the desired core–shell nanostructures. Unfortunately, making such seeds in solution synthesis commonly suffers from a complicated process. Moreover, spatial control of the solvent-dispersed NPs is challenging, which is highly demanded for advanced applications, including catalysis, metamaterials, and electronic and optical devices.

* Address correspondence to sangouk.kim@kaist.ac.kr, kwhokim@pusan.ac.kr.

Received for review March 17, 2015 and accepted April 20, 2015.

10.1021/acsnano.5b01641

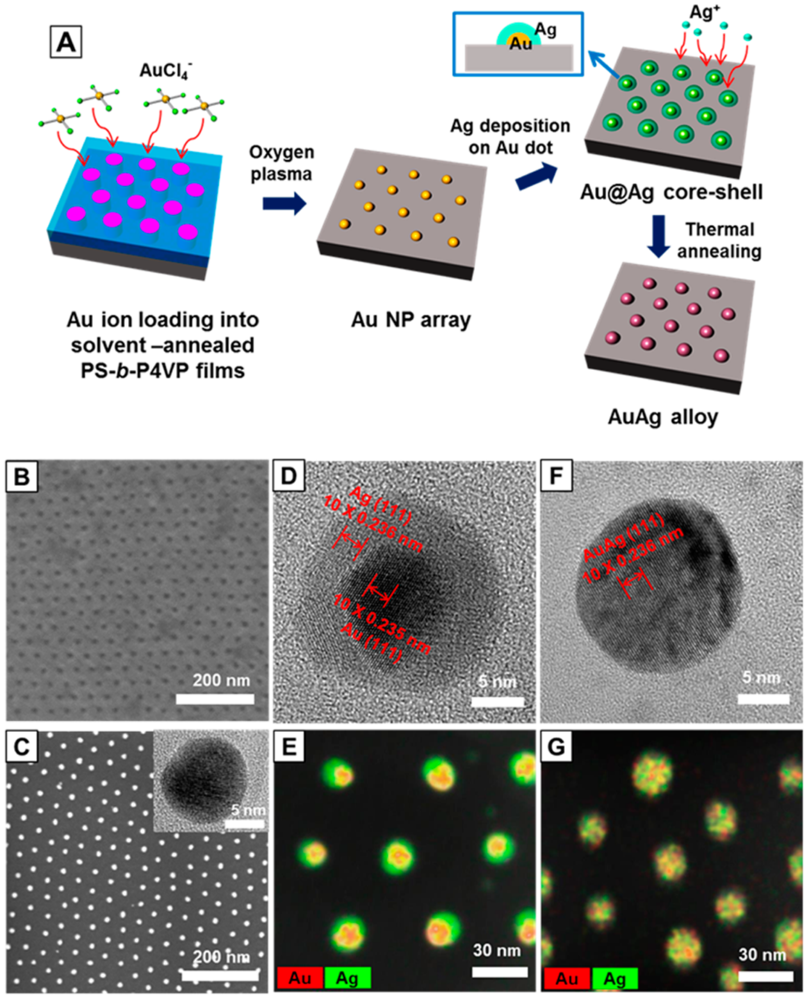

Figure 1. (A) Schematic illustration of Au@Ag core–shell and AuAg alloy nanopatterning process. (B) SEM image of solvent-annealed PS-*b*-P4VP thin film template. (C) SEM image of Au NPs. Inset shows the HRTEM image of the Au NP. (D) HRTEM image and (E) EDS elemental mapping of the Au@Ag core–shell NP array. (F) HRTEM image and (G) EDS elemental mapping of the AuAg alloy NP array.

We report a facile synthesis of highly ordered Au@Ag core–shell NP arrays using Au seeds prepared by block copolymer (BCP) lithography. BCP lithography is an effective method for large-area, well-ordered nanostructures with uniform size and shape.[35−47] Hexagonally arranged monodisperse Au nanoseeds formed by BCP lithography were further engineered for uniform and highly ordered Au@Ag NP arrays, whose shell thickness could be precisely controlled by reaction time. The resultant Au@Ag core–shell NP array with tunable core size, shell thickness, and spatial arrangement demonstrates the precise tunability of broadband LSPR properties over a wide range.

RESULTS AND DISCUSSION

Figure 1A illustrates the schematic procedure for the Au@Ag core–shell NP array. Asymmetric polystyrene-*block*-poly(4-vinylpyridine) (PS-*b*-P4VP, M_n = 37.5 kg/mol for PS and 16 kg/mol for P4VP) thin films were spin-cast onto a substrate. Solvent annealing under a toluene and tetrahydrofuran mixture induces vertically oriented hexagonal P4VP nanocylinder arrays enclosed by the PS matrix.[40,44,48−50] The self-assembled PS-*b*-P4VP thin films were immersed in $HAuCl_4$ acidic aqueous solution, where the protonated pyridinic nitrogen in P4VP blocks attracts negatively charged $AuCl_4^-$ complexes by electrostatic interaction. After the polymer thin film is removed by oxygen plasma etching, hexagonally ordered monodisperse Au NPs are left on the substrate.[40,43,44] Au@Ag core–shell NPs are grown from these Au NP seeds. The Au NP array is immersed in $AgNO_3$ aqueous solution with hydroquinone and cetyltrimethylammonium chloride (CTAC), which acted as reducing and capping agents, respectively.[19] Hydroquinone is the optimal reducing agent to fabricate well-aligned Au@Ag core–shell NP arrays due to fast reaction rate and selective Ag^+ reduction onto metal NPs.[51,52] Ag deposition on the Au seeds generates Au@Ag core–shell structure. The Ag shell thickness can be precisely controlled by immersing time in the $AgNO_3$ solution. Subsequent thermal annealing of the core–shell structure at a low temperature around

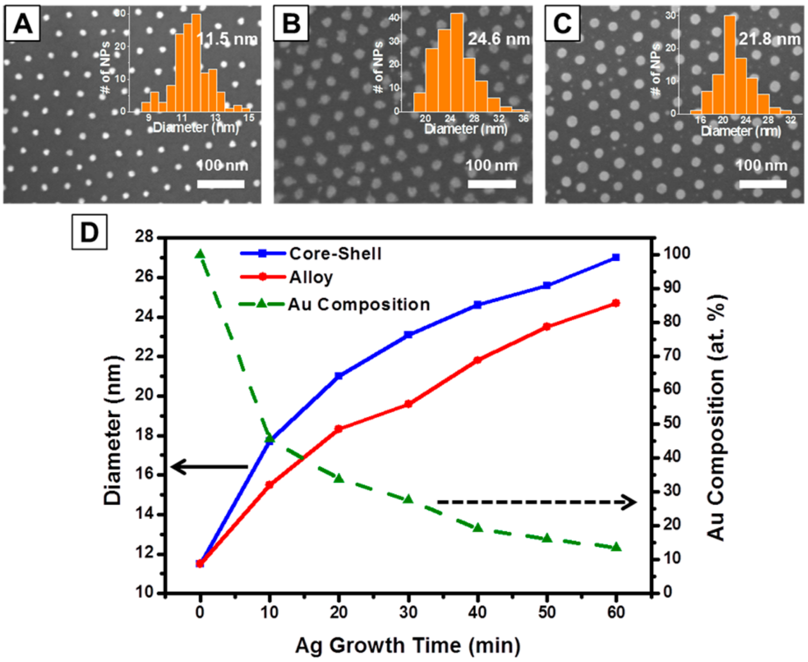

Figure 2. Tunability of bimetallic NP size and chemical composition. SEM images of (A) Au NP array, (B) Au@Ag core−shell NP array with the Ag shell growth time of 40 min, and (C) AuAg nanoalloy array transformed from (B) by thermal annealing. Insets represent their size distributions and average diameters. (D) Variation of average diameter and Au composition of core−shell and alloy NPs plotted against Ag shell growth time.

100 °C increases interdiffusion between Au and Ag and generates AuAg nanoalloy arrays, which are used as reference samples in this work.

Figure 1B presents the hexagonal vertical nanocylinder morphology of PS-*b*-P4VP thin film after solvent annealing. The cylindrical nanodomains have an average diameter of 17 nm with the periodicity (center to center distance) of 45 nm. Figure 1C shows Au nanoseed arrays replicating the BCP nanopattern morphology. The inset shows the single-crystalline nature of the Au seed. Upon immersion of Au nanoseeds in the Ag precursor solution, Ag^+ ions reduced by hydroquinone are specifically deposited at the Au seed surfaces. The Au nanoseeds have nanoscale curvature radii with large surface activities and a crystal structure similar to that of Ag, which greatly drives the selective heterogeneous nucleation principally at the Au seed surfaces (but not on the Si substrate).[53] Figure 1D shows the HRTEM (high-resolution transmission electron microscopy) image of a Au@Ag core−shell NP. The dark Au core is completely enclosed by the brighter Ag shell. Both metal layers exhibit a face-centered cubic phase with a few lattice mismatches (lattice constants of Au and Ag are 4.08 and 4.09 Å), which allows the epitaxial growth of Ag on the Au NP surface. The lattice spacings of Au and Ag are 0.235 and 0.236 nm, respectively, which correspond to the (111) *d*-spacing of each element.[54] Interestingly, the Ag shell surface shows less than 1 nm thick ultrathin oxide layer. At the interface between Au and Ag, charge redistribution may occur.[55−57] Au gains non-d-orbital electrons from Ag, while Ag gains d-orbital electrons from Au. The d-electrons of transition metals belong to the valence electrons that determine the chemical reactivity. As a result, d-electron transfer from the Au core may greatly retard the Ag oxidation. Such a low oxidation level is crucial for highly stable and strong plasmonic properties. Figure 1E shows the energy-dispersive X-ray spectroscopy (EDS) elemental mapping image of the Au@Ag core−shell NP array. The clear color contrast of Au (red) and Ag (green) confirms the core−shell structures. Figure 1F,G shows the HRTEM and EDS elemental mapping images of AuAg nanoalloys, where a homogeneous atomic mixing is observed. The (111) *d*-spacing of the AuAg nanoalloy is ~0.236 nm, close to pure Ag NPs, presumably due to the higher Ag composition (~55 atom %) (Supporting Information, Figure S1). Figure 1G shows that hexagonal ordering is still well-maintained after a thermal alloying process.

Figure 2A−C displays hexagonally ordered NP arrays of a pure Au seed, a Au@Ag core−shell, and a AuAg alloy, respectively. Well-aligned Au NPs with an average diameter of 11.5 nm (Figure 2A) could be exploited as nanoseeds for bimetallic structures. Au@Ag core−shell NPs (Figure 2B) were synthesized by Ag deposition for 40 min. Scanning electron microscopy (SEM) analysis reveals an average diameter of 24.6 nm and a standard deviation of 3.2 nm (13% of average diameter). Additional heat treatment of the core−shell NP array generates an alloy nanopattern with an average diameter of 21.8 nm and a standard deviation of 2.9 nm (Figure 2C). Figure 2D shows the size and

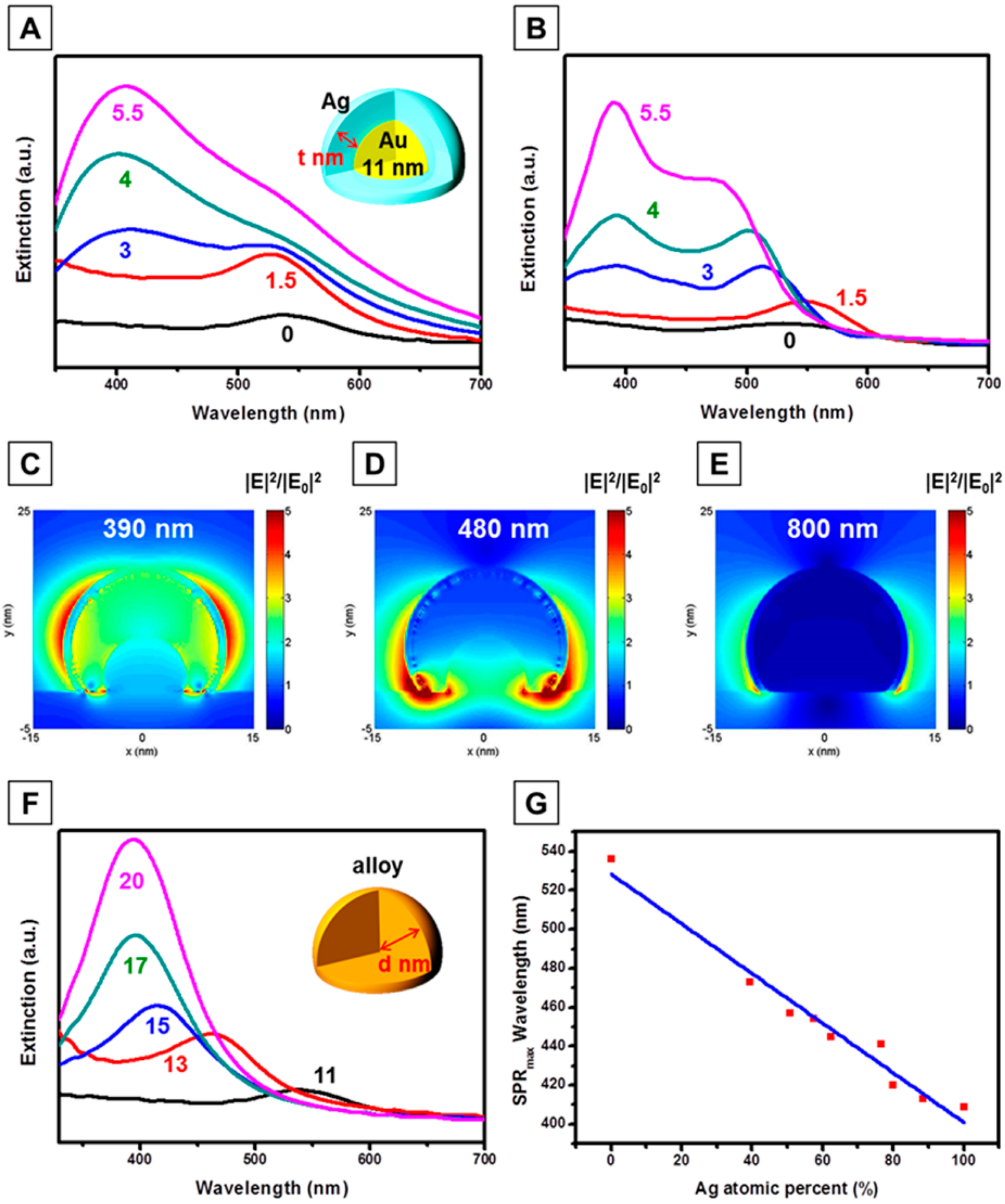

Figure 3. (A) UV−vis extinction spectra of the Au@Ag core−shell NP array with an 11 nm Au core and different Ag shell thicknesses (*t*) as indicated in the inset. (B) Calculated extinction spectra of the Au@Ag core−shell NP based on FDTD theory. Calculated electric field intensity profiles of the Au@Ag core−shell NP at wavelengths of (C) 390 nm, (D) 480 nm, and (E) 800 nm. (F) UV−vis extinction spectra of an alloy NP array with different diameter (*d*) as indicated in the inset. (G) Linear dependence between the SPR peak position and Ag composition in the nanoalloys.

composition change of NP arrays depending on Ag growth time (Supporting Information, Figure S2). The average diameter of Au@Ag core−shell NPs is widely controllable from 11 to 27 nm with Ag shell deposition time. The average diameter of AuAg nanoalloys becomes slightly smaller than the core−shell nanostructure. Such dimensional decrease is attributed to the shape change of NPs from hemisphere-like to sphere-like to reduce the surface energy during thermal annealing. Increasing the Ag shell growth time to longer than 1 h generates NPs larger than 30 nm but also causes the aggregation of NPs (Supporting Information, Figure S3). The dashed line in Figure 2D shows the relationship between Au composition and Ag shell growth time, characterized by XPS analysis. The decrease of relative Au composition principally occurs at the initial stage of reaction and gradually saturates with time. After 1 h of Ag deposition, Ag composition reaches ∼90 atom %. These results confirm the precise tunability of size and chemical composition in the bimetallic nanostructures.

The bimetallic NP arrays prepared in this work demonstrate highly pronounced plasmonic properties. Figure 3A shows the experimental extinction spectra of

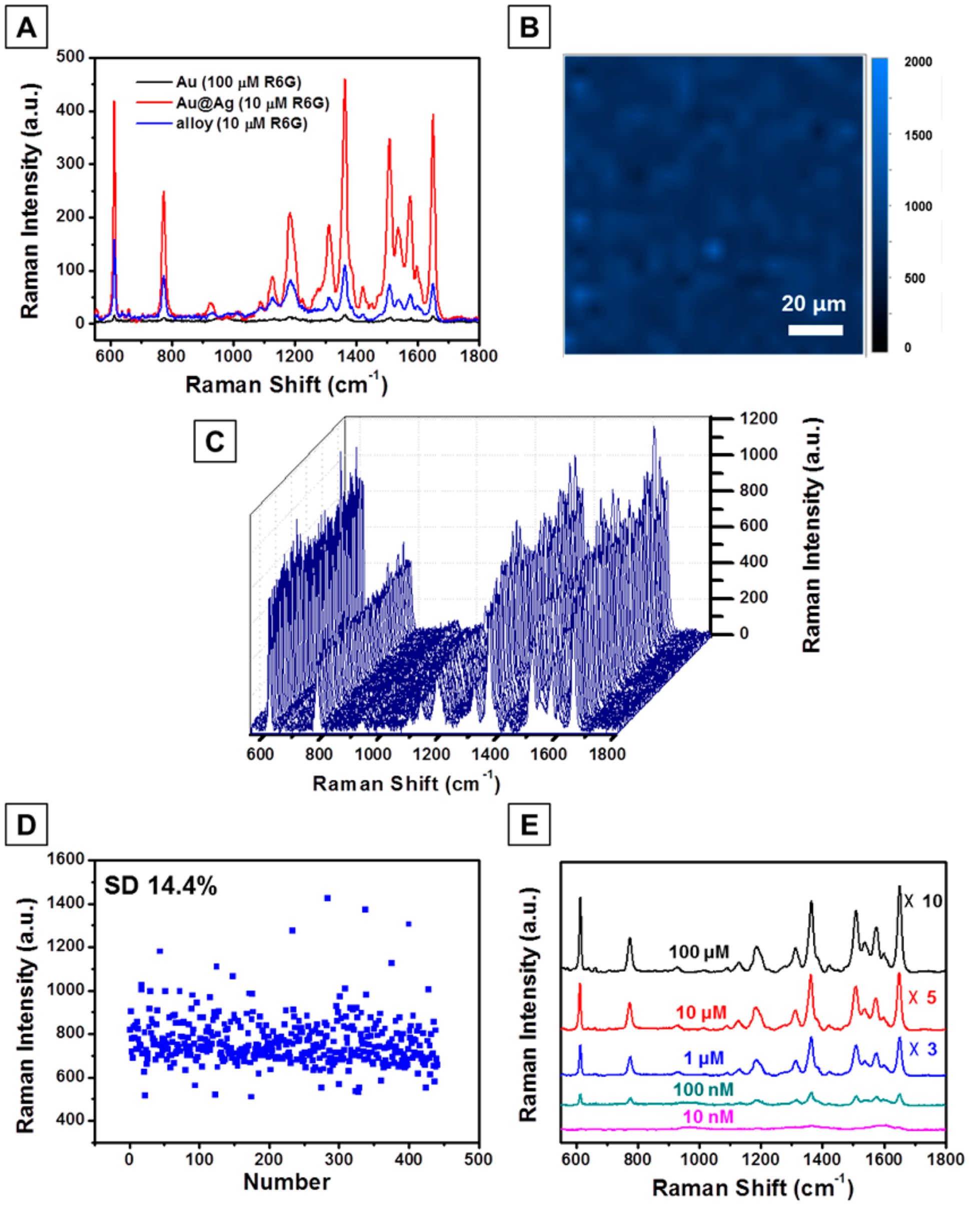

Figure 4. (A) Raman scattering spectra of R6G on pre-Au, Au@Ag core–shell, and AuAg alloy NP array substrates. (B) Raman mapping image of R6G on the Au@Ag core–shell NP array with a step size of 5 μm. (C) Raman scattering spectra of R6G on the area shown in (B). (D) Raman intensity distribution with standard deviations of 14.4% on the Au@Ag core–shell nanopattern. (E) Raman scattering spectra on the Au@Ag core–shell NP array with different R6G concentrations from 10 nM to 100 μM. A 514 nm excitation laser was used.

Au@Ag core–shell NP arrays with an 11 nm Au core and different Ag shell thicknesses (from 0 to 1.5, 3, 4, and 5.5 nm). The bare Au NP array has a LSPR peak around 540 nm. By contrast, Au@Ag core–shell NPs exhibit a broad LSPR peak combining the Au peak at 540 nm with the Ag peak at 400 nm. An increase of Ag shell thickness results in the systematic change of LSPR properties from Au-dominant to Ag-dominant characteristics with a gradual increase of peak intensity. The Au@Ag core–shell NPs with a shell thickness of 5.5 nm present an extinction peak intensity 8.5 times higher than that of Au NPs. This result is consistent with a numerical analysis based on a finite-difference time-domain (FDTD) calculation.[18,19,58] Figure 3B shows the extinction spectra simulated for the same structure shown in Figure 3A. A highly similar extinction tendency was predicted. However, Figure 3B exhibits more distinct peaks. This is attributed to the influence from the size and shape distribution of NPs. The minimal dispersibility in size and shape is unavoidable in the experimentally obtained NPs, while all NPs are assumed to have exactly the same size and idealized hemisphere shape in the simulation. An ensemble effect from different sizes and shapes causes the broad extinction spectra. Figure 3C–E represents the simulated electric field intensity profiles of a Au@Ag core–shell NP array with a shell thickness of 5.5 nm for different wavelengths. Figure 3C,D illustrates the intensified electric fields for 390 and 480 nm wavelength, respectively. It is obvious that two distinct resonances occur, which are dominated from Ag and Au components. The resonance induces strong absorption and scattering, which results in two extinction peaks, as shown in Figure 3B. In Figure 3E, by contrast, there is only a weak electric field enhancement around the NP for the incident light with a wavelength of 800 nm. Taken together, in the Au@Ag core–shell NP arrays, the LSPR properties in the visible wavelength range can be effectively controlled by Ag shell thickness.

AuAg nanoalloys present plasmonic properties entirely distinct from Au@Ag core–shell NPs. Figure 3F shows the experimental extinction spectra of AuAg alloy arrays formed by the thermal annealing of Au@Ag core–shell NP arrays. All AuAg nanoalloys with different diameters (from 11 to 13, 15, 17, and 20 nm) show single LSPR peaks unlike core–shell nanostructures. Interdiffusion of Au and Ag atoms during thermal annealing induces the homogeneous mixture phase of two metal elements. Notably, the blue shift of LSPR peaks is closely related to the atomic composition of nanoalloys. Figure 3G demonstrates the linear relationship between the LSPR wavelength and Ag composition in the nanoalloys. The LSPR wavelength is controllable from 540 to 400 nm with Ag atomic composition.

The strong LSPR effects of Au@Ag core–shell NP arrays are potentially useful for sensors, solar energy devices, bioimaging, and so on. We demonstrate the application to SERS substrates. The SERS substrates were simply prepared by dropping rhodamine 6G (R6G) dye molecule solution with different concentrations on the NP array samples. Figure 4A compares the Raman intensity spectra of R6G on pure Au, Au@Ag core–shell, and AuAg alloy NP arrays. Bimetallic NP arrays exhibit significant enhancement of Raman intensity, particularly for Au@Ag core–shell nanostructures. The Raman intensities of 10 μM R6G on the core–shell and alloy nanostructures at 1364 cm^{-1} are 460 and 111, respectively. By contrast, the Raman intensity on a pre-Au array is 17, despite the high concentration of R6G (100 μM). The Au@Ag core–shell NP array shows a Raman enhancement 270 times higher than that of pure Au, considering the concentration difference in R6G. Such an outstanding enhancement effect is attributed to the broadband surface plasmon resonance of Au@Ag core–shell NPs, which may effectively couple with a 514 nm laser used in Raman analysis.[18,59] The incident laser resonances with the surface plasmons at the Au@Ag core–shell NPs and this broadband LSPR effect considerably intensify the Raman signals of R6G. By contrast, the narrow plasmon resonance wavelength of AuAg alloy nanopattern is not exactly consistent with the wavelength of the laser such that the enhancement of Raman signal is much weaker than the core–shell structure.

Figure 4B shows the Raman intensity mapping image of R6G at 1362.5 cm^{-1} on a Au@Ag core–shell NP array. The Raman mapping was scanned over a 100 μm × 100 μm area with a step size of 5 μm. Highly uniform Raman intensity over a large area confirms that the observed SERS effect is reliable and applicable. Figure 4C demonstrates Raman intensity spectra obtained from Figure 4B, whose intensity distribution at 1362.5 cm^{-1} is presented in Figure 4D. Standard deviation of 14.4% over 400 points assures the fairly uniform SERS. Notably, our SERS substrate is easily scalable and reproducible with the genuine advantages of BCP lithography for reliable large-area patternability. Figure 4E exhibits Raman intensity spectra with different concentrations of R6G (from 10 nM to 100 μM) on Au@Ag core–shell NP arrays. It is possible to detect a very small amount of R6G down to the extent of 100 nM.

CONCLUSIONS

We have demonstrated a facile synthetic route to Au@Ag core–shell NP arrays exploiting BCP self-assembly and post-seeded growth. The bimetallic nanopatterns show the precise controllability of core–shell structure dimensions and composition along with the core formation and shell deposition conditions. The resultant synergistic tunable optical properties exhibit highly pronounced broadband surface plasmon resonances, which is obviously advantageous for SERS substrates and many other applications. The material composition of multicomponent nanopatterns can be readily extended to other metals and even ceramics. As such, multicomponent NP arrays are broadly useful for relevant applications, including plasmonics, catalysis, and energy storage devices.

METHODS

Materials. Asymmetric block copolymer, polystyrene-*block*-poly(4-vinylpyridine) (M_n = 37.5 kg/mol for PS and 16 kg/mol for P4VP) was purchased from Polymer Source, Inc. $HAuCl_4$ was purchased from Strem Chemicals. Toluene, tetrahydrofuran (THF), hydroquinone, cetyltrimethylammonium chloride solution (25 wt % in H_2O), and rhodamine 6G were purchased from Sigma-Aldrich. Silver nitrate was purchased from Kojima Chemicals Co., Ltd.

Preparation of the Au NP Array. Silicon wafers were immersed in a piranha solution (7:3 mixture of H_2SO_4 and H_2O_2) for 1 h at 110 °C and rinsed with deionized water several times. PS-*b*-P4VP BCP (0.5 wt %) was dissolved in a toluene/THF solvent mixture (3/1, w/w). The BCP solution was spin-cast on the piranha-treated silicon substrates. The prepared BCP thin films were solvent-annealed in a closed vessel saturated with toluene/THF (2/8, v/v) vapors for 6 h at room temperature. During the solvent annealing, perpendicularly ordered hexagonal nanocylinder domains were developed. The self-assembled BCP thin film templates were immersed in 3 mM $HAuCl_4$ acidic aqueous solution for 3 min to selectively deposit Au ionic precursors into P4VP cylinders. After Au precursor loading, the samples were rinsed with deionized water and dried with N_2 gas. Oxygen plasma treatment for 1 min completely removed the BCP, and hexagonally ordered Au nanoclusters were left on the substrate. Subsequent thermal annealing at 500 °C induces the agglomeration of Au nanoclusters and generates monodisperse Au NP arrays.

Fabrication of Au@Ag Core−Shell and AuAg Alloy NP Arrays. The prepared Au NP arrays were immersed in deionized water (1 L) at room temperature. Then, $AgNO_3$ (0.1 mM), hydroquinone (0.2 mM), and CTAC solution (0.1 mL) were simultaneously dissolved in the water with magnetic stirring. Au@Ag core−shell NPs with different shell thicknesses were formed depending on the immersion time. After deposition of the Ag shell for a given time, the core−shell samples were rinsed with deionized water and dried with N_2 gas. Au@Ag core−shell NPs were transformed into the AuAg nanoalloy by thermal annealing at 100 °C for 1 h.

TEM Sample Preparation. Au, Au@Ag, and AuAg alloy NP arrays formed on silicon substrates were directly observed by TEM analysis. Carbon was deposited on the samples to maintain NP ordering for further sample processing. The backsides of the sample substrates were polished out, and then the NP arrays on the thinned substrates were transferred to copper grids. Subsequent ion-milling makes 2−3 μm thin film samples that are appropriate for TEM analysis.

Surface-Enhanced Raman Scattering Analysis. Rhodamine 6G dye molecules were dissolved in ethanol with different concentrations (10 nM, 100 nM, 1 μM, 10 μM, and 100 μM). SERS substrates include Au, Au@Ag core−shell, and a AuAg alloy NP array (Ag growth time of 60 min) on the silicon substrates. For R6G deposition, 10 μL of R6G ethanol solutions was dropped on the SERS substrates, followed by the evaporation of ethanol solvent. A 514 nm laser was used in Raman scattering analysis. We randomly measured 10 different points on the R6G-dropped samples and averaged them to obtain reliable Raman scattering spectra.

Characterization. Au, Au@Ag core−shell, and AuAg alloy nanopatterns were imaged using a Hitachi S-4800 FE-SEM. HRTEM and EDS elemental mapping images of core−shell and alloy NPs were characterized by a Cs-corrected JEM-ARM200F HRTEM. Alloy compositions were analyzed by XPS (Thermo VG Scientific, Sigma Probe) measurements. The UV−vis extinction spectra were measured using a UV−vis spectrophotometer (Shimadzu, UV-2600). Raman spectroscopy was performed with ARAMIS (Horiba Jobin Yvon, France).

Finite-Difference Time-Domain Calculation. A commercial simulation tool with the FDTD algorithm of Yee was used to investigate the surrounding electric field vector and extinction properties of NPs numerically. The reliability of the FDTD algorithm was well-known. To make an exact model of the experimental situation, 0.1 nm mesh was used for NPs, and mesh size was gradually increased away from the NPs. Since the electromagnetic coupling between adjacent NPs is negligible, a simple square lattice of NPs was used in the simulation. The lateral and vertical boundary conditions were periodic and perfectly matched layer boundary, respectively, and four-fold symmetry was used. The dimension of the NPs and lattice parameter were determined from experimental measurement. The Ag shell had a 1 nm thick oxide layer. The tabulated electrical permittivity values were used for oxides, Au,[60] and Ag.[61]

Conflict of Interest: The authors declare no competing financial interest.

Acknowledgment. This research was supported by Global Frontier Program through the Global Frontier Hybrid Interface Materials (GFHIM) of the National Research Foundation of Korea (NRF) funded by the Ministry of Science, ICT & Future Planning (2014M3A6B1075032), and Institute for Basic Science (IBS-R004-D1-2015-a00).

Supporting Information Available: Additional supporting research results. This material is available free of charge *via* the Internet at http://pubs.acs.org.

REFERENCES AND NOTES

1. Tao, A.; Sinsermsuksakul, P.; Yang, P. Polyhedral Silver Nanocrystals with Distinct Scattering Signatures. *Angew. Chem., Int. Ed.* **2006**, *45*, 4597–4601.
2. Wei, Q. H.; Su, K. H.; Durant, S.; Zhang, X. Plasmon Resonance of Finite One-Dimensional Au Nanoparticle Chains. *Nano Lett.* **2004**, *4*, 1067–1071.
3. Zhang, J.; Liu, H.; Wang, Z.; Ming, N. Shape-Selective Synthesis of Gold Nanoparticles with Controlled Sizes, Shapes, and Plasmon Resonances. *Adv. Funct. Mater.* **2007**, *17*, 3295–3303.
4. Jin, R.; Cao, Y. C.; Hao, E.; Metraux, G. S.; Schatz, G. C.; Mirkin, C. A. Controlling Anisotropic Nanoparticle Growth through Plasmon Excitation. *Nature* **2003**, *425*, 487–490.
5. Caruso, F.; Spasova, M.; Salgueiriño-Maceira, V.; Liz-Marzán, L. M. Multilayer Assemblies of Silica-Encapsulated Gold Nanoparticles on Decomposable Colloid Templates. *Adv. Mater.* **2001**, *13*, 1090–1094.
6. Maillard, M.; Giorgio, S.; Pileni, M. P. Silver Nanodisks. *Adv. Mater.* **2002**, *14*, 1084–1086.
7. Lal, S.; Link, S.; Halas, N. J. Nano-optics from Sensing to Waveguiding. *Nat. Photonics* **2007**, *1*, 641–648.
8. Sonnichsen, C.; Reinhard, B. M.; Liphardt, J.; Alivisatos, A. P. A Molecular Ruler Based on Plasmon Coupling of Single Gold and Silver Nanoparticles. *Nat. Biotechnol.* **2005**, *23*, 741–745.
9. Mirkin, C. A.; Letsinger, R. L.; Mucic, R. C.; Storhoff, J. J. A DNA-Based Method for Rationally Assembling Nanoparticles into Macroscopic Materials. *Nature* **1996**, *382*, 607–609.
10. Lee, J.-S.; Ulmann, P. A.; Han, M. S.; Mirkin, C. A. A DNA−Gold Nanoparticle-Based Colorimetric Competition Assay for the Detection of Cysteine. *Nano Lett.* **2008**, *8*, 529–533.
11. Hao, F.; Nordlander, P.; Sonnefraud, Y.; Dorpe, P. V.; Maier, S. A. Tunability of Subradiant Dipolar and Fano-Type Plasmon Resonances in Metallic Ring/Disk Cavities: Implications for Nanoscale Optical Sensing. *ACS Nano* **2009**, *3*, 643–652.
12. Zeng, J.; Zhang, Q.; Chen, J.; Xia, Y. A Comparison Study of the Catalytic Properties of Au-Based Nanocages, Nanoboxes, and Nanoparticles. *Nano Lett.* **2010**, *10*, 30–35.
13. Slater, T. J. A.; Macedo, A.; Schroeder, S. L. M.; Burke, M. G.; O'Brien, P.; Camargo, P. H. C.; Haigh, S. J. Correlating Catalytic Activity of Ag−Au Nanoparticles with 3D Compositional Variations. *Nano Lett.* **2014**, *14*, 1921–1926.
14. Nie, S.; Emory, S. R. Probing Single Molecules and Single Nanoparticles by Surface-Enhanced Raman Scattering. *Science* **1997**, *275*, 1102–1106.
15. Mulvihill, M. J.; Ling, X. Y.; Henzie, J.; Yang, P. Anisotropic Etching of Silver Nanoparticles for Plasmonic Structures Capable of Single-Particle SERS. *J. Am. Chem. Soc.* **2009**, *132*, 268–274.
16. Cho, W. J.; Kim, Y.; Kim, J. K. Ultrahigh-Density Array of Silver Nanoclusters for SERS Substrate with High Sensitivity and Excellent Reproducibility. *ACS Nano* **2011**, *6*, 249–255.
17. Tao, A.; Kim, F.; Hess, C.; Goldberger, J.; He, R.; Sun, Y.; Xia, Y.; Yang, P. Langmuir−Blodgett Silver Nanowire Monolayers for Molecular Sensing Using Surface-Enhanced Raman Spectroscopy. *Nano Lett.* **2003**, *3*, 1229–1233.
18. Samal, A. K.; Polavarapu, L.; Rodal-Cedeira, S.; Liz-Marzán, L. M.; Pérez-Juste, J.; Pastoriza-Santos, I. Size Tunable Au@Ag Core−Shell Nanoparticles: Synthesis and Surface-Enhanced Raman Scattering Properties. *Langmuir* **2013**, *29*, 15076–15082.
19. Ma, Y.; Li, W.; Cho, E. C.; Li, Z.; Yu, T.; Zeng, J.; Xie, Z.; Xia, Y. Au@Ag Core−Shell Nanocubes with Finely Tuned and Well-Controlled Sizes, Shell Thicknesses, and Optical Properties. *ACS Nano* **2010**, *4*, 6725–6734.

20. Wang, C.; Peng, S.; Chan, R.; Sun, S. Synthesis of AuAg Alloy Nanoparticles from Core/Shell-Structured Ag/Au. *Small* **2009**, *5*, 567–570.
21. Shore, M. S.; Wang, J.; Johnston-Peck, A. C.; Oldenburg, A. L.; Tracy, J. B. Synthesis of Au (Core)/Ag (Shell) Nanoparticles and Their Conversion to AuAg Alloy Nanoparticles. *Small* **2011**, *7*, 230–234.
22. Peng, Z.; Yang, H. Designer Platinum Nanoparticles: Control of Shape, Composition in Alloy, Nanostructure and Electrocatalytic Property. *Nano Today* **2009**, *4*, 143–164.
23. Li, Y.; Li, L.; Liao, H.; Wang, H. Preparation of Pure Nickel, Cobalt, Nickel−Cobalt and Nickel−Copper Alloys by Hydrothermal Reduction. *J. Mater. Chem.* **1999**, *9*, 2675–2677.
24. Sra, A. K.; Schaak, R. E. Synthesis of Atomically Ordered AuCu and AuCu$_3$ Nanocrystals from Bimetallic Nanoparticle Precursors. *J. Am. Chem. Soc.* **2004**, *126*, 6667–6672.
25. Wang, C.; Yin, H.; Chan, R.; Peng, S.; Dai, S.; Sun, S. One-Pot Synthesis of Oleylamine Coated AuAg Alloy NPs and Their Catalysis for CO Oxidation. *Chem. Mater.* **2009**, *21*, 433–435.
26. Peng, Z.; You, H.; Yang, H. Composition-Dependent Formation of Platinum Silver Nanowires. *ACS Nano* **2010**, *4*, 1501–1510.
27. Sun, S.; Murray, C. B.; Weller, D.; Folks, L.; Moser, A. Monodisperse FePt Nanoparticles and Ferromagnetic FePt Nanocrystal Superlattices. *Science* **2000**, *287*, 1989–1992.
28. Wang, C.; Hou, Y.; Kim, J.; Sun, S. A General Strategy for Synthesizing FePt Nanowires and Nanorods. *Angew. Chem., Int. Ed.* **2007**, *46*, 6333–6335.
29. Sun, Y.; Mayers, B. T.; Xia, Y. Template-Engaged Replacement Reaction: A One-Step Approach to the Large-Scale Synthesis of Metal Nanostructures with Hollow Interiors. *Nano Lett.* **2002**, *2*, 481–485.
30. Sun, Y.; Mayers, B.; Xia, Y. Metal Nanostructures with Hollow Interiors. *Adv. Mater.* **2003**, *15*, 641–646.
31. Hong, J. W.; Kang, S. W.; Choi, B.-S.; Kim, D.; Lee, S. B.; Han, S. W. Controlled Synthesis of Pd−Pt Alloy Hollow Nanostructures with Enhanced Catalytic Activities for Oxygen Reduction. *ACS Nano* **2012**, *6*, 2410–2419.
32. Lu, C.-L.; Prasad, K. S.; Wu, H.-L.; Ho, J.-a. A.; Huang, M. H. Au Nanocube-Directed Fabrication of Au−Pd Core−Shell Nanocrystals with Tetrahexahedral, Concave Octahedral, and Octahedral Structures and Their Electrocatalytic Activity. *J. Am. Chem. Soc.* **2010**, *132*, 14546–14553.
33. Lu, Y.; Zhao, Y.; Yu, L.; Dong, L.; Shi, C.; Hu, M. J.; Xu, Y. J.; Wen, L. P.; Yu, S. H. Hydrophilic Co@Au Yolk/Shell Nanospheres: Synthesis, Assembly, and Application to Gene Delivery. *Adv. Mater.* **2010**, *22*, 1407–1411.
34. Habas, S. E.; Lee, H.; Radmilovic, V.; Somorjai, G. A.; Yang, P. Shaping Binary Metal Nanocrystals through Epitaxial Seeded Growth. *Nat. Mater.* **2007**, *6*, 692–697.
35. Park, M.; Harrison, C.; Chaikin, P. M.; Register, R. A.; Adamson, D. H. Block Copolymer Lithography: Periodic Arrays of $\sim 10^{11}$ Holes in 1 Square Centimeter. *Science* **1997**, *276*, 1401–1404.
36. Kim, S. O.; Solak, H. H.; Stoykovich, M. P.; Ferrier, N. J.; de Pablo, J. J.; Nealey, P. F. Epitaxial Self-Assembly of Block Copolymers on Lithographically Defined Nanopatterned Substrates. *Nature* **2003**, *424*, 411–414.
37. Stoykovich, M. P.; Müller, M.; Kim, S. O.; Solak, H. H.; Edwards, E. W.; De Pablo, J. J.; Nealey, P. F. Directed Assembly of Block Copolymer Blends into Nonregular Device-Oriented Structures. *Science* **2005**, *308*, 1442–1446.
38. Chai, J.; Wang, D.; Fan, X.; Buriak, J. M. Assembly of Aligned Linear Metallic Patterns on Silicon. *Nat. Nanotechnol.* **2007**, *2*, 500–506.
39. Thurn-Albrecht, T.; Schotter, J.; Kästle, G. A.; Emley, N.; Shibauchi, T.; Krusin-Elbaum, L.; Guarini, K.; Black, C. T.; Tuominen, M. T.; Russell, T. P. Ultrahigh-Density Nanowire Arrays Grown in Self-Assembled Diblock Copolymer Templates. *Science* **2000**, *290*, 2126–2129.
40. Shin, D. O.; Lee, D. H.; Moon, H. S.; Jeong, S. J.; Kim, J. Y.; Mun, J. H.; Cho, H.; Park, S.; Kim, S. O. Sub-nanometer Level Size Tuning of a Monodisperse Nanoparticle Array *via* Block Copolymer Lithography. *Adv. Funct. Mater.* **2011**, *21*, 250–254.
41. Tang, C.; Lennon, E. M.; Fredrickson, G. H.; Kramer, E. J.; Hawker, C. J. Evolution of Block Copolymer Lithography to Highly Ordered Square Arrays. *Science* **2008**, *322*, 429–432.
42. Cheng, J. Y.; Mayes, A. M.; Ross, C. A. Nanostructure Engineering by Templated Self-Assembly of Block Copolymers. *Nat. Mater.* **2004**, *3*, 823–828.
43. Mun, J. H.; Chang, Y. H.; Shin, D. O.; Yoon, J. M.; Choi, D. S.; Lee, K.-M.; Kim, J. Y.; Cha, S. K.; Lee, J. Y.; Jeong, J.-R.; et al. Monodisperse Pattern Nanoalloying for Synergistic Intermetallic Catalysis. *Nano Lett.* **2013**, *13*, 5720–5726.
44. Shin, D. O.; Mun, J. H.; Hwang, G.-T.; Yoon, J. M.; Kim, J. Y.; Yun, J. M.; Yang, Y.-B.; Oh, Y.; Lee, J. Y.; Shin, J.; et al. Multicomponent Nanopatterns by Directed Block Copolymer Self-Assembly. *ACS Nano* **2013**, *7*, 8899–8907.
45. Peng, Q.; Tseng, Y.-C.; Darling, S. B.; Elam, J. W. Nanoscopic Patterned Materials with Tunable Dimensions *via* Atomic Layer Deposition on Block Copolymers. *Adv. Mater.* **2010**, *22*, 5129–5133.
46. Peng, Q.; Tseng, Y.-C.; Darling, S. B.; Elam, J. W. A Route to Nanoscopic Materials *via* Sequential Infiltration Synthesis on Block Copolymer Templates. *ACS Nano* **2011**, *5*, 4600–4606.
47. Tseng, Y.-C.; Peng, Q.; Ocola, L. E.; Elam, J. W.; Darling, S. B. Enhanced Block Copolymer Lithography Using Sequential Infiltration Synthesis. *J. Phys. Chem. C* **2011**, *115*, 17725–17729.
48. Park, S.; Wang, J.-Y.; Kim, B.; Chen, W.; Russell, T. P. Solvent-Induced Transition from Micelles in Solution to Cylindrical Microdomains in Diblock Copolymer Thin Films. *Macromolecules* **2007**, *40*, 9059–9063.
49. Park, S.; Lee, D. H.; Xu, J.; Kim, B.; Hong, S. W.; Jeong, U.; Xu, T.; Russell, T. P. Macroscopic 10-Terabit-per-Square-Inch Arrays from Block Copolymers with Lateral Order. *Science* **2009**, *323*, 1030–1033.
50. Kim, S. H.; Misner, M. J.; Xu, T.; Kimura, M.; Russell, T. P. Highly Oriented and Ordered Arrays from Block Copolymers *via* Solvent Evaporation. *Adv. Mater.* **2004**, *16*, 226–231.
51. Gentry, S. T.; Fredericks, S. J.; Krchnavek, R. Controlled Particle Growth of Silver Sols through the Use of Hydroquinone as a Selective Reducing Agent. *Langmuir* **2009**, *25*, 2613–2621.
52. Lim, D.-K.; Kim, I.-J.; Nam, J.-M. DNA-Embedded Au/Ag Core−Shell Nanoparticles. *Chem. Commun.* **2008**, 5312–5314.
53. Wang, D.; Li, Y. Bimetallic Nanocrystals: Liquid-Phase Synthesis and Catalytic Applications. *Adv. Mater.* **2011**, *23*, 1044–1060.
54. Wang, A.-Q.; Liu, J.-H.; Lin, S.; Lin, T.-S.; Mou, C.-Y. A Novel Efficient Au−Ag Alloy Catalyst System: Preparation, Activity, and Characterization. *J. Catal.* **2005**, *233*, 186–197.
55. Anh, D. T. N.; Singh, P.; Shankar, C.; Mott, D.; Maenosono, S. Charge-Transfer-Induced Suppression of Galvanic Replacement and Synthesis of (Au@Ag)@Au Double Shell Nanoparticles for Highly Uniform, Robust and Sensitive Bioprobes. *Appl. Phys. Lett.* **2011**, *99*, 073107.
56. Shankar, C.; Dao, A. T.; Singh, P.; Higashimine, K.; Mott, D. M.; Maenosono, S. Chemical Stabilization of Gold Coated by Silver Core−Shell Nanoparticles *via* Electron Transfer. *Nanotechnology* **2012**, *23*, 245704.
57. Tyson, C.; Bzowski, A.; Kristof, P.; Kuhn, M.; Sammynaiken, R.; Sham, T. Charge Redistribution in Au−Ag Alloys from a Local Perspective. *Phys. Rev. B* **1992**, *45*, 8924.
58. Bao, Z.; Sun, Z.; Xiao, M.; Chen, H.; Tian, L.; Wang, J. Transverse Oxidation of Gold Nanorods Assisted by Selective End Capping of Silver Oxide. *J. Mater. Chem.* **2011**, *21*, 11537–11543.
59. Lee, W.; Lee, S. Y.; Briber, R. M.; Rabin, O. Self-Assembled SERS Substrates with Tunable Surface Plasmon Resonances. *Adv. Funct. Mater.* **2011**, *21*, 3424–3429.
60. Johnson, P. B.; Christy, R.-W. Optical Constants of the Noble Metals. *Phys. Rev. B* **1972**, *6*, 4370.
61. Palik, E. D. *Handbook of Optical Constants of Solids*; Academic Press: New York, 1997.